Multiphysics Evaluation of High-Speed SynRM and PMa-SynRM Rare-Earth-Less Permanent Magnets for Automotive Traction ⋆

Gabriel B. da Silveira * **Igor P. Wiltuschnig** * **Aurélio T Salton** *
Letícia G. Tobias dos Santos ** **Cristiano de A. Soares** **
and Paulo R. Eckert *

* *Universidade Federal do Rio Grande do Sul (UFRGS), Porto Alegre, Brazil*
** *Mercosul Industria de motores S.A.*

Abstract:
This paper presents a multiphysics evaluation of a Synchronous Reluctance Motor (SynRM) and a Ferrite Permanent Magnet-Assisted Synchronous Reluctance Motor (PMa-SynRM), both featuring a liquid-cooled housing. Initially, the study discusses the effects of the PM assistance, assessing its impact on flux linkages and inductances within the d-q reference frame. An experimental test is proposed to determine the rated current density that can be used for the stator windings with the current cooling system. Additionally, the paper analyzes the performance of both motors using a maximum torque per ampere (MTPA) control strategy and the experimentally determined rated current density. Finally, the mechanical reliability of the rotor is verified through numerical simulations of tension and radial expansion to ensure reliable operation from a base speed of 6,000 rpm up to 12,000 rpm.

Keywords: Multiphysics Evaluation, High-speed, Liquid Cooling, PMa-SynRM, SynRM.

1. INTRODUCTION

There is an increasing need for high-efficiency motors rare-earth less permanent magnets or with a reduced volume of them, particullary in automotive traction applications. In order to meet these requirements, Synchronous Reluctance Motors (SynRM) are an attractive option due to their significant field weakening and overload capability, high efficiency and low production costs (Murataliyev et al. (2022)). Additionally, SynRM do not require permanent magnets to work. Despite their benefits, several investigations are still looking into problems like (i) enhancing torque and power density, (ii) maximizing power factor, and (iii) maintaining mechanical reliability at high speeds.

Eletromagenetic torque is generally proportional to both electrical and magnetic loadings. In practice, increasing the torque requires enhancing the electrical loading, as the magnetic loading is constrained by iron saturation at high flux densities. There are two main ways to increase electric loading: increasing the current density in the windings or using a higher copper filling factor, as with hairpin windings (Berardi and Bianchi (2018)). The first, leads to higher temperatures in the stator windings due to increased current densities, while the second adds complexity and higher costs to the manufacturing process. Analytical and numerical models can be employed to predict temperature rise and ensure that the motor operates within its thermal limits (Ragazzo et al. (2020); Ding et al. (2022)).

The SynRM is typically described using the synchronous d–q reference frame, where the ratio between the direct L_d and quadrature L_q inductances is known as saliency ξ. In order to increase the saliency, the magnetic flux along the q-axis are obstructed using flux barriers in the rotor. On the other hand, these flux barriers experience significant stress at high speeds, which may lead to their deformation and possible radial expansion. A collision with the stator could result from this expansion and may lead to mechanical failure. To ensure reliable operation at high speeds, bridges can be used to reinforce the mechanical structure of the rotor. Mechanical models can predict the radial forces on the bridges and determine their optimal width (Ma et al. (2024); Li et al. (2023)).

Bridges can enhance structural reliability but also facilitates magnetic flux along the q-axis, which reduces saliency and consequently decreases torque. The power factor (PF) of SynRM is inherently low and can be further worsened by the number, dimensions and position of the bridges. To address this issue, several strategies can be employed. Key approaches include adding permanent magnets to the rotor to saturate the bridges and improve saliency (López-Torres et al. (2018); Stipetic et al. (2020)); and utilizing a maximum power factor (MPF) control strategy to enhance the PF through the electrical angle (Shahin et al. (2023); Lin et al. (2020)).

⋆ This work was supported in part by Fundação de Desenvolvimento da Pesquisa (Fundep) under Rota 2030 Program - Linha V Proc. 27192.03.01/2022.04-00 - and in part by the National Council for Scientific and Technological Development (CNPq) under Grant 303643/2023-4 - and in part by the Coordenação de Aperfeiçoamento de Pessoal de Nível Superior - Brasil (CAPES) - Finance Code 001.

A mechanical analysis is required to determine the viability of using a SynRM in vehicle traction applications due to the complicated geometry of the rotor, which must be optimized to withstand huge radial forces. The current density must match the cooling system's capacity, necessitating a thermal analysis. Finally, the electromagnetic analysis must verify if the performance, in terms of torque and power densities, is sufficient to meet the application requirements. The following sections evaluate the performance and reliability of a SynRM and PMa-SynRM.

2. ELECTROMAGNETIC PERFORMANCE

This section highlights the differences in electromagnetic performance due to the permanent magnet assistance in the evaluated motors. It begins with a summary of the main parameters and material definitions. Following this, an electromagnetic comparison is conducted by analyzing a custom .DFX geometry using Ansys-MotorCAD.

2.1 Description of the Motors

The stator is equipped with hairpin windings, which allow for a higher copper fill factor in the slots. As a result, this enhances the electrical loading at the same current density compared to conventional windings. The rotor has sufficient space to accommodate permanent magnets, which, for this study, are made of ferrite. The parameters of the motors are shown in Table 1. As indicated, the active part has an outer diameter of 210 mm, which corresponds to a NEMA 132 housing dimension. The demagnetization and initial magnetization curves of the magnets and electrical steel were characterized by the authors and used in the simulation. The mechanical proprieties of the electrical steel are shown in the Table 2. The main parts of the SynRM are indicated in Figure 1.

Table 1. Parameter of the Evaluated SynRM and PMa-SynRM.

Name	Value	unit
DC-bus voltage	800	V
Phase supply voltage	325	V
Number of poles	4	-
Base speed	6000	rpm
Maximum speed	12000	rpm
Axial length	210	mm
Stator outer diameter	210	mm
Stator inner diameter	132	mm
Airgap	0.5	mm
Rotor outer diameter	131	mm
Rotor inner diameter	40	mm
Number of slots	48	-
Slot fill factor	0.7	-
Turns per coil	3	-
Number of coils per phase	8	-
Turns in series per phase	24	-
Paralels path	2	-

Table 2. Mechanical Proprieties of the Electrical Steel.

Name	Value	unit
Poisson's Ratio	0.28	-
Young's Coefficient	165	GPa
Yield Stress	425	MPa

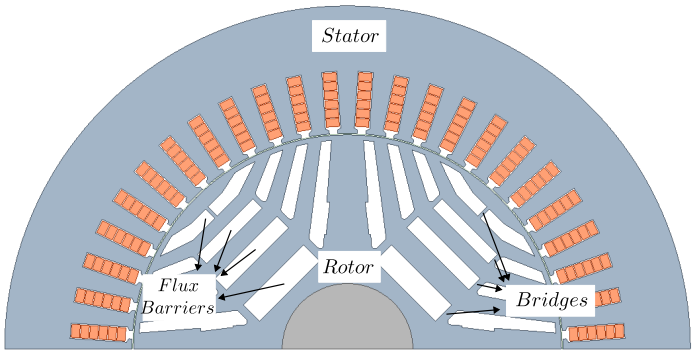

Figure 1. Main parts of the SynRM.

2.2 The SynRM and the Permanent Magnet-Assistance

Synchronous $d-q$ reference frame is usually used to represent the SynRM. Figure 2a illustrates the axes and rotor of the SynRM, while Figure 2b shows the PMa-SynRM. The red arrows indicate the direction of magnetization of the magnets. It is important to note that the magnets are typically positioned along the q-axis in an opposing configuration.

The electromagnetic torque, as described by Equation (1), is primarily proportional to the reluctance component $(L_d - L_q) \cdot i_d i_q$. Meanwhile, the term $\psi_m \cdot i_d$ represents the magnetic torque and depends on the amount of permanent magnets in the flux barriers. The saliency ξ, defined as shown in Equation (2), affects the torque by highlighting the difference between L_d and L_q, thereby increasing the reluctance component.

$$T_e = \frac{3}{2} \cdot p[\psi_m \cdot i_d + (L_d - L_q) \cdot i_d i_q] \tag{1}$$

$$\xi = L_d / L_q \tag{2}$$

Figure 3 shows the vector diagram of the reluctance motor. In Figure 3a, it is possible to observe that the component $-\omega L_q i_q$ determines the angle ϕ between the voltage $\vec{V}$ and current $\vec{I}$, which directly impacts the power factor. The power factor in a SynRM can also be determined using the saliency ξ, as shown in Equation 3.

$$FP = \frac{(\xi + 1)}{(\xi - 1)} \tag{3}$$

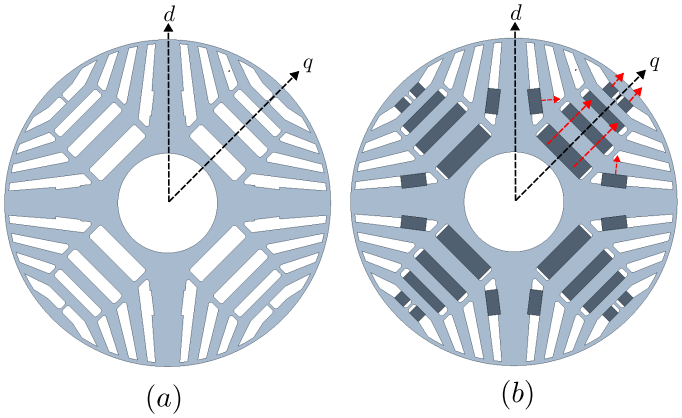

Figure 2. Rotor geometry of the evaluated motor. (a) SynRM. (b) PMa-SynRM.

As shown in Figure 3b, when the permanent magnet is positioned along the q-axis, the voltage vector rotates towards the current vector, resulting in an increased power factor as $FP = cos(\phi)$. Additionally, the permanent magnet saturates the rotor bridges, which decreases the magnetic permeability along the q-axis and consequently reduces the inductance L_q.

Figures 4 and 5 illustrate the effects of permanent magnet assistance from the perspectives of flux lines and bridge saturation. The first image shows that a significant portion of the magnetic flux generated by the magnets remains confined within the rotor, with only a small fraction crossing the air gap towards the stator. Meanwhile, the second image clearly demonstrates the effect of bridge saturation, indicating that the magnets are effectively achieving their intended purpose.

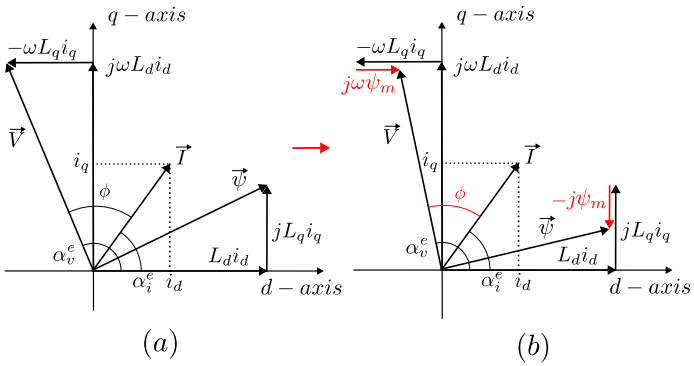

Figure 3. Vector diagram. (a) SynRM. (b) PMa-SynRM.

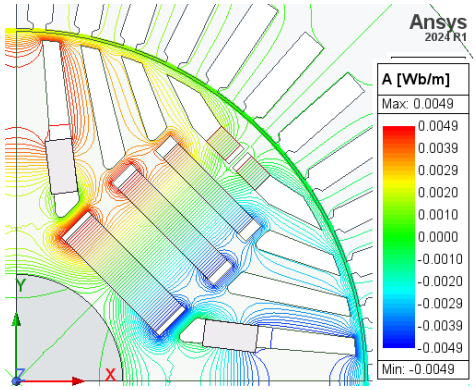

Figure 4. Flux lines map of the PMa-SynRM Due to PM.

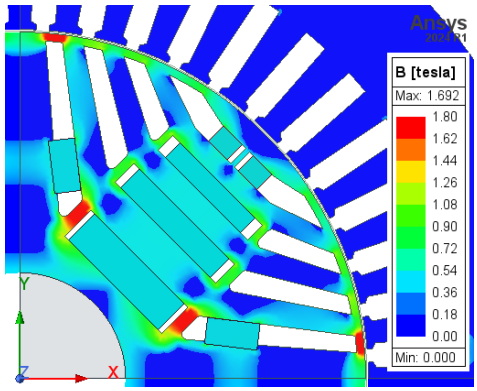

Figure 5. Flux density of the PMa-SynRM due to PM.

The $d-q$ flux linkages ψ_{dq} can be determinated using the equations (4) and (5). In a SynRM, the flux along the q-axis ψ_q is consistently lower than that along the d-axis ψ_d. This is primarily because the q-axis is the path with lower permeability in the rotor, so L_q has a lower value than L_d. In a PMa-SynRM, the q-flux ψ_q tends to be even lower due to the opposing magnetic flux from the permanent magnets ψ_m and the further reduction in permeability caused by bridge saturation.

$$\psi_d = L_d \cdot i_d \tag{4}$$

$$\psi_q = L_q \cdot i_q - \psi_m \tag{5}$$

Figure 6 shows the d-axis flux linkage ψ_d (with $i_q = 0$) and the q-axis flux linkage ψ_q (with $i_d = 0$) as functions of current density for the evaluated motors. It is evident that, at all considered current densities, the ψ_d is consistently higher than ψ_q due to the effects previously discussed. Moreover, the ψ_q in the PMa-SynRM is significantly reduced due to the permanent magnet assistance.

The inductances L_d for maximum magnetic coupling (with $i_q = 0$) and L_q for minimum magnetic coupling (with $i_d = 0$) are presented in Figure 7. It is possible to conclude that in the PMa-SynRM, along with the expected effect of increased PF due to increased saliency ξ, the torque T_e will also experience a slight increase. This occours because, in addition to the reluctance torque, which will rise according to Equation (1), there will be torque contribution due to the permanent magnet-assistance.

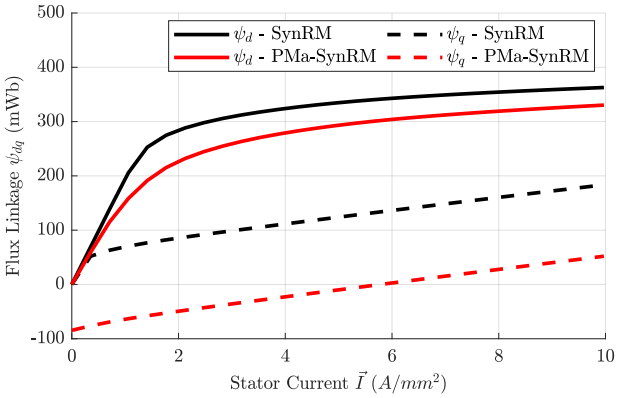

Figure 6. Flux linkage of the SynRM and PMa-SynRM.

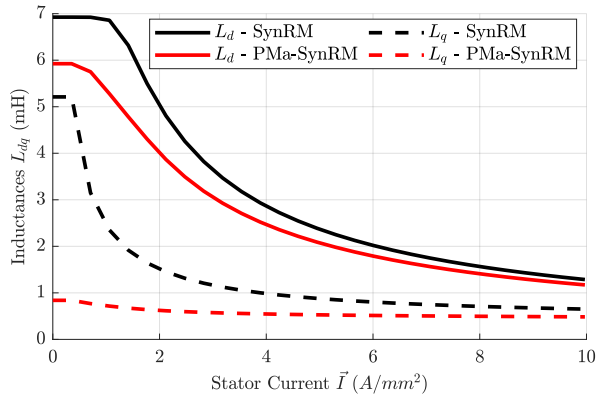

Figure 7. Inductances of the SynRM and PMa-SynRM.

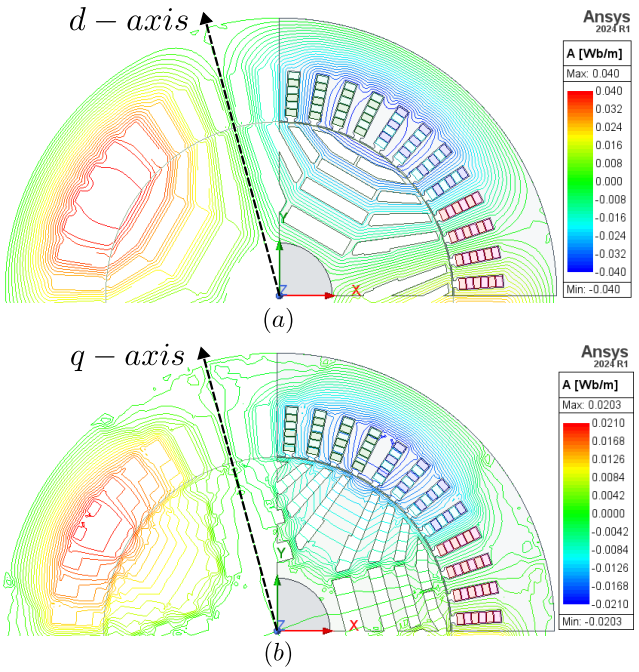

Figure 8. d-q flux lines of the SynRM. (a) d-axis ($i_q = 0$). (b) q-axis ($i_d = 0$).

In Figure 8, the flux lines in the paths of maximum magnetic coupling (d-axis with $i_q = 0$) and minimum (q-axis with $i_d = 0$) are illustrated for a current density of 10 A/mm^2 in the windings. The next section proposes an experimental procedure to establish the electrical loading limits of an electric motor with a liquid-cooled housing by examining the relationship between current density and temperature rise at the coil heads.

3. ELECTRICAL LOADING LIMITS BASED ON TEMPERATURE RISE

Evaluating a cooling system can be done through computational fluid dynamics (CFD) analysis, analytical models and by experimental tests. These methods attempt to predict temperature increases caused by heat sources, such as electrical losses in the stator windings and magnetic losses. This study focuses on experimentally assessing the electrical loading limits of a liquid-cooled housing. Details of the conducted tests and the parameters used to determine a safe rated current density are discussed as follows.

3.1 Prototype

Figure 9 shows the prototype housing currently undergoing evaluation. It utilizes an indirect cooling system where the windings are not cooled directly. Instead, heat is transferred to the housing primarily through conduction. The cooling fluid, entering through the inlet, follows an axial path, circulates around the housing, and exits through the outlet, dissipating heat via convection. Typically, systems with forced ventilation can safely operate up to a current density of 5 A/mm^2. Therefore, the goal of these tests is to determine a safe current density value for the liquid-cooled system and ensure proper heat dissipation.

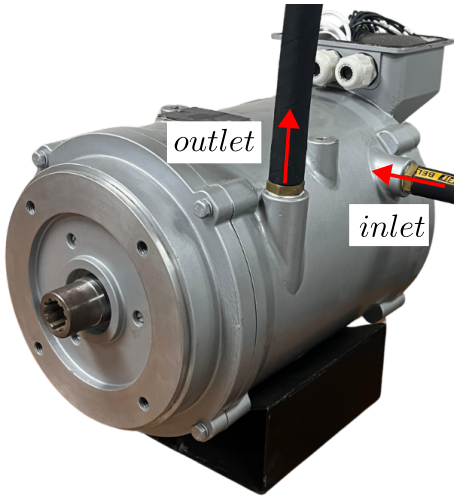

Figure 9. Prototype of the liquid-cooled housing.

3.2 Experimental Test Procedure

Due to the operating principle of the SynRM, most of the heat generated comes from Joule losses in the stator windings, followed by magnetic losses and other minor losses. Moreover, the rotor and ferrite magnets are resistant to thermal effects and typically do not encounter temperature issues. Therefore, to assess the thermal performance of the prototype, heat generated from Joule losses is used. During the the experiments, the heat source comes from a DC current passing through a 3-phase winding of an industrial motor (IR3 efficiency rating), as can be seen in Figure 10.

The windings are connected in series to ensure uniform current density across all of them, as illustrated in the circuit shown in Figure 11. Additionally, PT100 temperature sensors are positioned on each phase at the coil heads. These areas often become thermal hotspots in radial flux electric motors. This happens because the coil heads do not have direct contact with the active parts of the stator, and the air around them is a poor thermal conductor. Consequently, the temperature rise at the coil heads is consistently higher compared to the temperature of the copper within the slots.

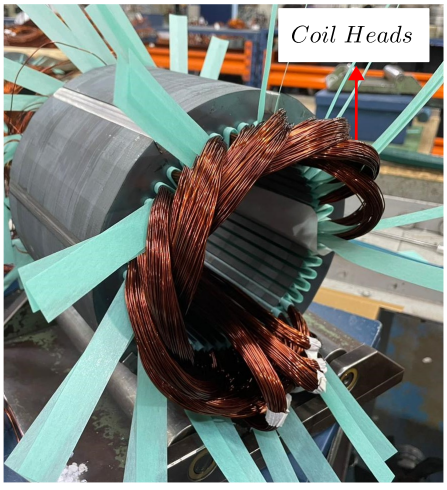

Figure 10. Mounting of the stator used as a heat source.

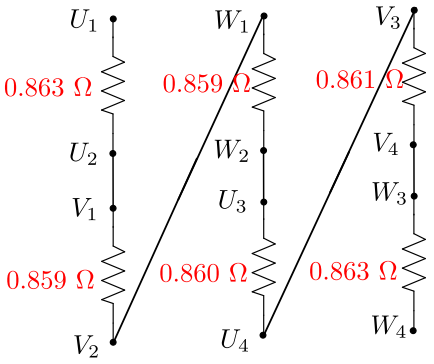

Figure 11. Electrical connections of the windings.

3.3 Hydraulic Path and Data Aquisition

The system is cooled using water at a flow rate of 20 L/min, with real-time monitoring provided by an SMC PF3W740 flow sensor. A 3-phase pump, controlled by an inverter, maintains a consistent flow through a SAE 100 3/4" hydraulic hose. Water enters through the inlet, cools the housing, and exits through the outlet, where it is then further cooled by an automotive radiator. The hydraulic path is illustrated in Figure 12 and the experimental layout is shown in Figure 13.

In addition to the temperature sensors at the coil heads, PT100 sensors were installed at the inlet and outlet of the prototype to measure the temperature rise of the water. The resistance variations of these sensors are converted into a voltage signal ranging from 0 to 10 V using a transmitter. This voltage signal is then read by an analog input of a MicroLabBox. An interface was developed in the ControlDesk to interpret the analog signal, allowing for real-time monitoring of temperature increases during the tests.

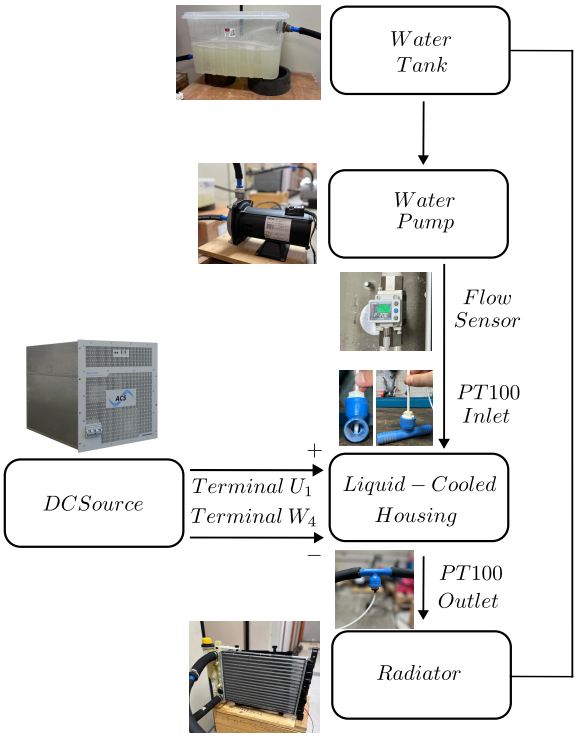

Figure 12. Scheme of the hidraulic path.

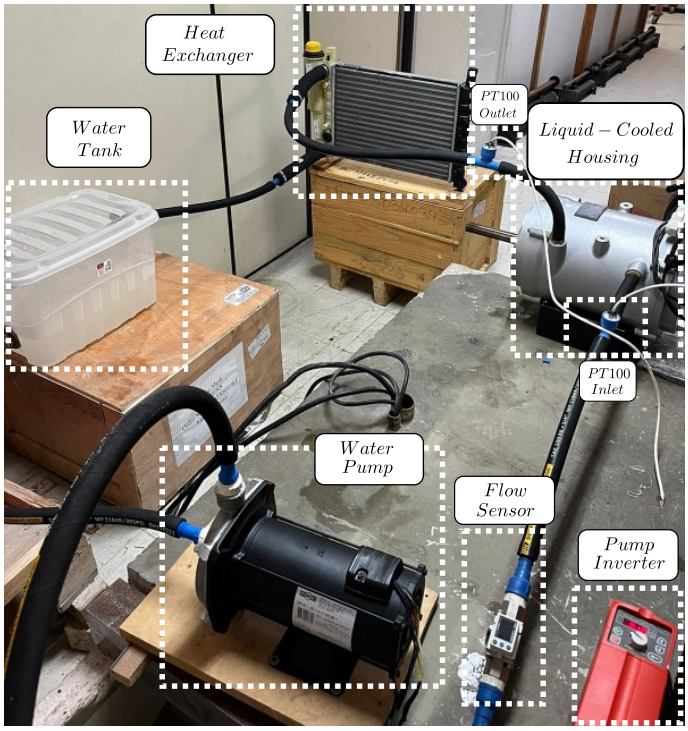

Figure 13. Experimental test layout.

To generate the electrical power needed for the heat source, a TC.ACS full four-quadrant three-phase AC source was utilized. This device enables programmable waveform configuration suited to the test requirements. For this setup, a DC current control function was used. The current value is regulated via an analog input on the TC.ACS, which reads an analog signal transmitted by the MicrolabBox. Desired current values are inputted into the ControlDesk interface, allowing the operator to make adjustments as needed.

3.4 Results of the Temperature Rising

The initial temperature at the coil heads was recorded at 28 ^oC, with ambient conditions reaching 35 ^oC on the test day. The tests began at a current density of 5 and progressed up to 12 A/mm^2. Measurements were taken at steady state, with each current density value being stabilized for 20 minutes to ensure accurate temperature readings. The test room heated up as a result of the extended test duration and the restricted thermal exchange between the environment and the exterior. So the results are trustworthy even on hot days.

Figure 14 illustrates the relationship between temperature and current density. Given that the winding insulation used in the stator is Class F (155°C), thermal limits were observed at a current density of 12 A/mm², with temperatures at the coil heads reaching 157°C. Figure 15 presents an image taken with a thermal camera, which measured a temperature of 156°C at the coil heads. This measurement is consistent with the readings from the temperature sensors.

The Table 3 provides the applied values for current, voltage, equivalent resistance, and power. As can be seen, the resistance value increase with temperature, highlighting a critical issue: higher temperatures cause greater resistance,

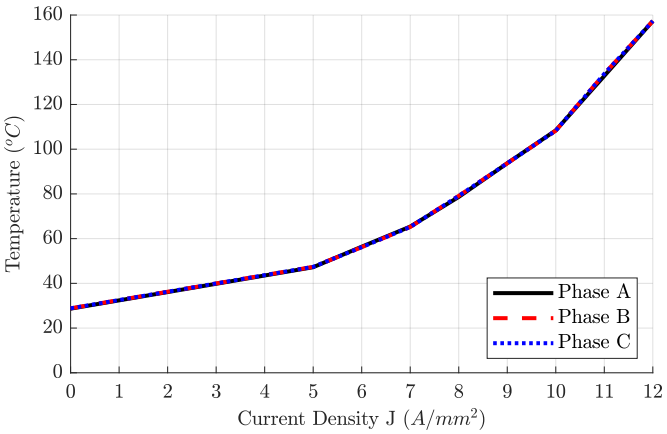

Figure 14. Temperature rise of the coil heads.

Figure 15. Temperature under a 12 A/mm^2 condition.

Table 3. Electrical measurements of the experimental test.

Current (A/mm^2)	Voltage (V)	Current (A)	Power (W)	Resistance (Ω)
Initial	0	0	0	5.25
5	41.19	7.25	300	5.71
6	53.18	8.64	430	5.76
7	65.54	10.11	601	5.88
8	77.94	11.58	820	6.12
9	82.29	13.08	1076	6.29
10	94.73	14.52	1372	6.51
11	109.2	15.91	1737	6.86
12	125.42	17.4	2183	7.21

leading to increased losses and additional heat generation. Consequently, considering the extra losses and heat produced under load conditions, a safe rated current density for reliable operation with this cooling system is determined to be 10 A/mm^2. This can ensure that the system remains within the thermal limits of both the copper windings and the slot insulation.

The next section analyzes the motors' performance in terms of power and torque densities at the rated condition. The evaluation also includes examining the motors under a Maximum Torque Per Ampere (MTPA) strategy, assessing their performance at a base speed of 6000 rpm and under flux weakening conditions to achieve a maximum speed of 12000 rpm. Additionally, the mechanical reliability of the rotor is evaluated by discussing the tension and expansion experienced in both operating conditions, ensuring that the design can withstand the associated mechanical stresses.

4. RESULTS AND DISCUSSIONS

This section presents results based on the numerical model discussed in Section 2, applying a current density of 10 A/mm^2 to evaluate performance and assess the impact of permanent magnet-assistance. Ansys-MotorCAD was used to generate saturation and loss maps, while the LAB model was employed to implement a Maximum Torque Per Ampere (MTPA) control strategy. The mechanical model is also used to evaluate the radial efforts acting on the rotor.

4.1 Rated Performance

Table 4 presents a comparative analysis of the rated performance of the SynRM and PMa-SynRM. The Pma-SynRM exhibits an increase in shaft torque to 184.42 Nm, up by 19.68 Nm from the SynRM's 164.74 Nm. Additionally, the Pma-SynRM achieves a power factor of 0.71, compared to 0.62 for the SynRM. This higher power factor reflects the Pma-SynRM's improved efficiency in converting electrical power into mechanical power, resulting in reduced reactive power consumption and the need for a smaller inverter.

Both motors exhibit high efficiency, with the Pma-SynRM achieving 97.36 % compared to 96.78 % for the SynRM. It is important to note that these efficiency values do not account for losses from the cooling system, as windage losses are excluded and thermal effects are considered only at the windings. The results are based on a winding temperature of 110°C, with the phase resistance adjusted to reflect this condition.

Torque ripple can lead to vibrations and audible noise, and the table shows a value of 69.28 Nm, corresponding

Table 4. Performance rated of the evaluated SynRM and PMa-SynRM.

Name	SynRM	Pma-SynRM	Unit
Phase Resistance	20.41	20.36	mΩ
D-axis Inductance	2.43	2.458	mH
Q-axis Inductance	0.5341	0.5871	mH
Shaft Torque	164.74	184.42	Nm
Torque Ripple	69.28	50.76	Nm
Torque Ripple	41.71	27.39	%
Power Factor	0.62	0.71	-
Input Power	106.95	119.01	kW
Total Losses	3437.8	3133.2	W
Output Power	103.51	115.88	kW
Efficiency	96.78	97.36	%
Specific Torque	2,01	3,21	kNm/kg
Specific Power	1,86	2,01	kW/kg
Torque Density	3.94	4.42	kNm/m^3
Power density	2.47	2.76	MW/m^3

to 41.71 %. This is a high level of ripple and can impact motor performance and operational comfort. Although tests involving rotor segmented skewing reduced the ripple to less than 10 %, this analysis will not be explored further in this study. The PMa-SynRM exhibits a torque ripple of 27.39 % without skewing, reflecting a reduction due to the rotor's optimization for permanent magnet assistance.

4.2 Performance driving MTPA control Strategy

The Figure 16 presents a comparison of the average torque and power of both motors under MTPA control strategy. Solid lines represent torque, while dashed lines indicate power. The results show that both motors can sustain the discussed torque values at speeds up to 6900 rpm, while staying within the inverter voltage limits and operating with a modulation index of 1. At this point, the SynRM motor achieves a power output of 126 kW, whereas the PMa-SynRM produces up to 146 kW.

Achieving speeds up to 12,000 rpm requires field weakening, with an attempt to maintain constant power output. While it was expected that the SynRM would struggle to maintain constant power, the PMa-SynRM also faces similar difficulties. This is due to the lower energy product of ferrite magnets, which are susceptible to permanent demagnetization from armature reaction. Despite this, the power output of the PMa-SynRM remains above the rated value at 6,000 rpm throughout the entire field weakening range.

Figures 17 displays the power factor maps for both motors on the same scale. The results show that the PM-assisted motor enhances the power factor across all ranges of torque and speed, reaching a maximum value of 0.84. This represents an improvement of 0.15 over the SynRM, which has a maximum power factor of 0.69. In vehicular applications, this improvement translates to better battery efficiency during highway trips, as the motor operates in a field weakening mode in this case.

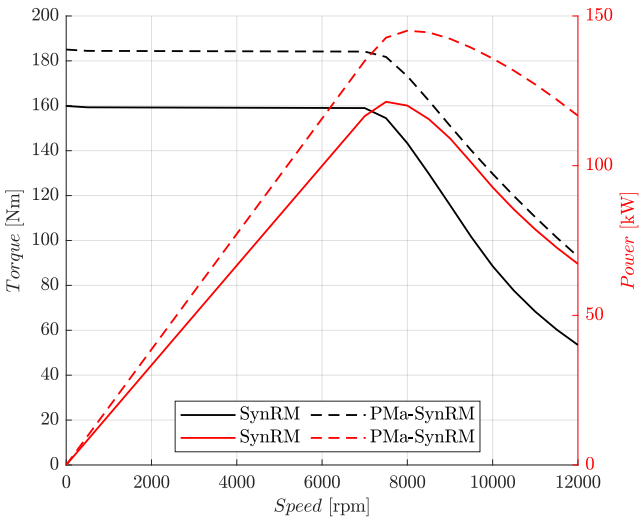

Figure 16. Torque and power under MTPA condition.

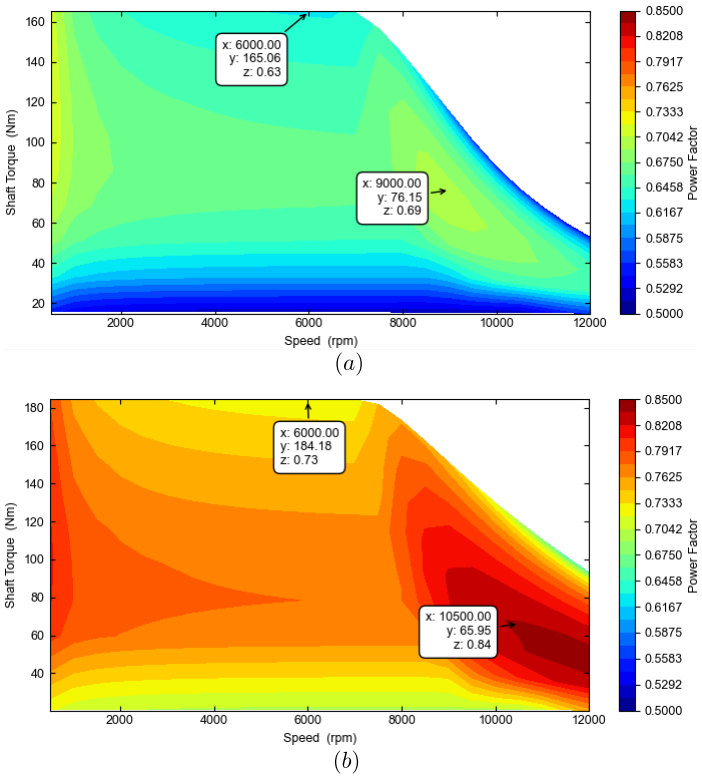

Figure 17. PF map. (a) SynRM. (b) PMa-SynRM.

4.3 Mechanical reliability

Figure 18 illustrates the tension and displacement of the rotor at maximum speed, representing the worst-case scenario in terms of radial force incidence. It is evident that employing a double bridge on the flux barriers is an effective approach, as it distributes the forces across the barriers and limits the maximum tension to 387 MPa. According to Table 1, the yield stress of the steel is 425 MPa, indicating that the rotor operates within the elastic deformation range. Table 5 shows detailed results for base and maximum speed operation.

The bridges narrow towards the airgap because the inner bridges support the weight of all the barriers and permanent magnets. This design strategy optimizes performance by balancing structural support with minimizing reductions in torque and power factor, as wider barriers can negatively impact electromagnetic performance. Additionally, since the machine does not undergo plastic deformation, the maximum displacement is 39.11 μm, ensuring that the rotor returns to its original position. With an air gap of 0.5 mm, this design effectively prevents any contact between the rotor and stator.

Table 5. Mechanical results of the evaluated motors at base and maximum speed.

Name	SynRM		Pma-SynRM		Unit
	base	max.	base	max	
Tension (max)	106.14	338.51	117.25	387.13	MPa
Safety Factor	4.01	1.25	3.63	1.09	-
Displacement (max)	8.24	32.97	9.77	39.11	μm

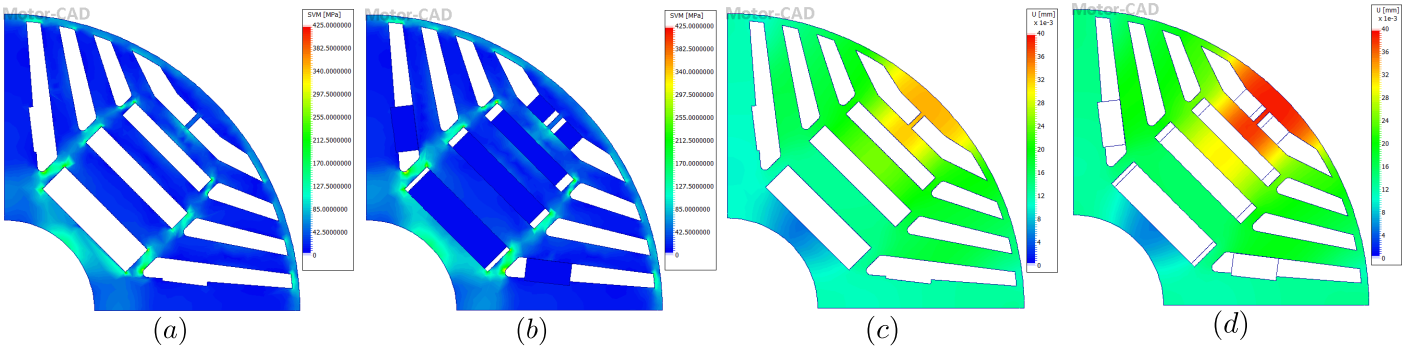

Figure 18. Tension and displacement of the rotor at 12000 rpm. (a) SynRM (tension). (b) PMa-SynRM (tension). (c) SynRM (displacement). (d) PMa-SynRM (displacement).

5. CONCLUSIONS

The PMa-SynRM demonstrates superior torque capabilities and a higher power factor throughout the entire speed range, achieving a maximum value of 0.84 compared to 0.69 for the SynRM. This improvement reflects a significant gain in power conversion efficiency, which is especially beneficial for vehicular applications. Additionally, the PMa-SynRM demonstrates superior output power compared to the SynRM throughout the field weakening range. While it was anticipated that the SynRM would struggle to maintain constant power, the expectation was that the PMa-SynRM would perform better. However, the PMa-SynRM also encounters challenges in maintaining constant power at speeds above 6,900 rpm. This difficulty arises due to the high current density and the lower energy product of ferrite magnets, which are susceptible to irreversible demagnetization. Despite this, the PMa-SynRM shows reduced torque ripple, attributable to its rotor design optimized for permanent magnet-assistance. These findings underscore the benefits of permanent magnet in the motor and suggest areas for further research, including strategies for mitigating torque ripple, vibration, and noise, to fully realize their potential.

REFERENCES

Berardi, G. and Bianchi, N. (2018). Design guideline of an ac hairpin winding. In *2018 XIII International Conference on Electrical Machines (ICEM)*, 2444–2450. doi:10.1109/ICELMACH.2018.8506785.

Ding, L., Ju, X., Cui, S., and Cheng, Y. (2022). Hybrid modeling method for thermal analysis of hairpin winding permanent magnet machine. In *2022 IEEE 5th International Electrical and Energy Conference (CIEEC)*, 2965–2969. doi:10.1109/CIEEC54735.2022.9845908.

Li, Y., Ma, B., Zheng, J., Zhu, J., and Lei, G. (2023). Electromagnetic and mechanical topology optimization for synrm rotors considering high dimensional constraints. *IEEE Transactions on Industrial Electronics*, 70(12), 12048–12059. doi:10.1109/TIE.2023.3234146.

Lin, F.J., Chen, S.G., and Liang, C.H. (2020). Online maximum power factor searching control for synchronous reluctance motor based on current angle control. In *2020 15th IEEE Conference on Industrial Electronics and Applications (ICIEA)*, 278–283. doi:10.1109/ICIEA48937.2020.9248401.

López-Torres, C., Garcia Espinosa, A., Riba, J.R., and Romeral, L. (2018). Design and optimization for vehicle driving cycle of rare-earth-free synrm based on coupled lumped thermal and magnetic networks. *IEEE Transactions on Vehicular Technology*, 67(1), 196–205. doi:10.1109/TVT.2017.2739020.

Ma, B., Li, Y., Zheng, J., Zhang, J., Huang, S., Zhu, J., and Lei, G. (2024). Multiphysics topology optimization of synrms considering control performance and machinability. *IEEE Transactions on Transportation Electrification*, 1–1. doi:10.1109/TTE.2024.3400846.

Murataliyev, M., Degano, M., Di Nardo, M., Bianchi, N., and Gerada, C. (2022). Synchronous reluctance machines: A comprehensive review and technology comparison. *Proceedings of the IEEE*, 110(3), 382–399. doi:10.1109/JPROC.2022.3145662.

Ragazzo, P., Ferrari, S., Rivière, N., Popescu, M., and Pellegrino, G. (2020). Efficient multiphysics design workflow of synchronous reluctance motors. In *2020 International Conference on Electrical Machines (ICEM)*, volume 1, 2507–2513. doi:10.1109/ICEM49940.2020.9270670.

Shahin, A., Nair, D.S., Shreelakshmi, M.P., and Ramchand, R. (2023). Design and analysis of maximum power factor control for a three phase synchronous reluctance motor. In *2023 5th Global Power, Energy and Communication Conference (GPECOM)*, 181–186. doi:10.1109/GPECOM58364.2023.10175803.

Stipetic, S., Zarko, D., and Cavar, N. (2020). Adjustment of rated current and power factor in a synchronous reluctance motor optimally designed for maximum saliency ratio. *IEEE Transactions on Industry Applications*, 56(3), 2481–2490. doi:10.1109/TIA.2020.2971442.